

See discussions, stats, and author profiles for this publication at: <https://www.researchgate.net/publication/5278908>

Spectroscopic Definition of the Ferroxidase Site in M Ferritin: Comparison of Binuclear Substrate vs Cofactor Active Sites

ARTICLE *in* JOURNAL OF THE AMERICAN CHEMICAL SOCIETY · AUGUST 2008

Impact Factor: 12.11 · DOI: 10.1021/ja801251q · Source: PubMed

CITATIONS

34

READS

21

5 AUTHORS, INCLUDING:



Jennifer Kathleen Schwartz

Stanford University

17 PUBLICATIONS 420 CITATIONS

SEE PROFILE



Takehiko Tosha

SPring-8

58 PUBLICATIONS 1,247 CITATIONS

SEE PROFILE



Elizabeth C Theil

North Carolina State Univ., Raleigh, NC; & Chi...

209 PUBLICATIONS 8,202 CITATIONS

SEE PROFILE

Published in final edited form as:

J Am Chem Soc. 2008 July 23; 130(29): 9441–9450. doi:10.1021/ja801251q.

Spectroscopic Definition of the Ferroxidase Site in M Ferritin: Comparison of Binuclear Substrate vs. Cofactor Active Sites

Jennifer K. Schwartz¹, Xiaofeng S. Liu², Takehiko Tosha², Elizabeth C. Theil^{2,*}, and Edward I. Solomon^{1,*}

¹Department of Chemistry, Stanford University, 333 Campus Drive, Stanford, California 94305

²Center for BioIron at CHORI (Children's Hospital Oakland Research Institute), 747 52nd Street, Oakland, California 94609

Abstract

Maxi ferritins, 24 subunit protein nanocages, are essential in humans, plants, bacteria, and other animals for the concentration and storage of iron as hydrated ferric oxide, while minimizing free radical generation or use by pathogens. Formation of the precursors to these ferric oxides is catalyzed at a non-heme biferrous substrate site, which has some parallels with the cofactor sites in other biferrous enzymes. A combination of circular dichroism (CD), magnetic circular dichroism (MCD), and variable-temperature, variable-field MCD (VTVH MCD) has been used to probe Fe(II) binding to the substrate active site in frog M ferritin. These data determined that the active site within each subunit consists of two inequivalent five-coordinate (5C) ferrous centers that are weakly anti-ferromagnetically coupled, consistent with a μ -1,3 carboxylate bridge. The active site ligand set is unusual and likely includes a terminal water bound to each Fe(II) center. The Fe(II) ions bind to the active sites in a concerted manner, and cooperativity among the sites in each subunit is observed, potentially providing a mechanism for the control of ferritin iron loading. Differences in geometric and electronic structure – including a weak ligand field, availability of two water ligands at the biferrous substrate site, and the single carboxylate bridge in ferritin – coincide with the divergent reaction pathways observed between this substrate site and the previously studied cofactor active sites.

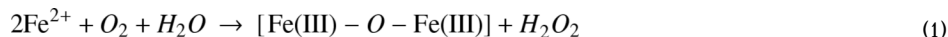
I. Introduction

Binuclear non-heme iron enzymes catalyze a variety of reactions using a largely conserved ligand set at the active site. Most studied of these include ribonucleotide reductase (R2), which converts ribonucleotide into deoxyribonucleotides, Δ^9 desaturase (Δ^9 d), which inserts a double bond into a fatty acid chain, and methane monooxygenase (MMO), which catalyzes the oxidation of methane to methanol. Spectroscopic¹⁻⁴ and crystallographic studies⁵⁻⁷ of these proteins have shown that the catalytic sites contain two Fe(II) atoms that are weakly coupled through two bridging carboxylate ligands, and act as cofactors, i.e. are retained at the active site after the catalytic cycle. Dioxygen reacts with Fe(II) in the catalytic sites to form diferric peroxo intermediates, and, in at least MMO and R2, these convert to high-valent intermediates.⁸⁻¹¹

The ferritins are protein nanocages with binuclear active sites accommodating two Fe(II) *substrate* atoms. The substrate atoms catalytically react with dioxygen to form diferric oxo/hydroxo complex products released at the end of this oxidation cycle. These complexes are

*To whom correspondence should be addressed: etheil@chori.org and edward.solomon@stanford.edu.

precursors to the hydrated ferric oxo mineral stored in the ferritin nanocage cavity.¹² The rapid catalytic reaction occurring at the substrate site may be written as equation 1 with a fraction of the H₂O₂ released,¹² while the remainder reacts with mineral intermediates.¹³



Certain characteristics of the diferric peroxo intermediate (DFP) of this reaction,¹⁴⁻¹⁷ and the ligand set at one of the two Fe sites, are similar to those found in other binuclear non-heme iron enzymes, but the second Fe site is unique to ferritin.¹⁸ Fe(II) binding and the catalytic reaction with dioxygen that is characteristic of the maxi-ferritins of animals, plants, and bacteria, occurs at sites within the four-alpha-helix bundles of H and H' (M) subunits; animals are unusual in having a second type of subunit that is catalytically inactive, called L.¹² In maxi-ferritins, 24 polypeptide subunits self-assemble in O symmetry to form the spherical protein that is 120Å in diameter with an 80Å hollow core, theoretically capable of storing up to 4500 iron atoms as hydrated ferric mineral. The symmetrical assembly of subunits produces hydrophilic channels at the three-fold axes, postulated to allow entry and exit of the Fe(II) ions, and hydrophobic channels at the four-fold axes. The function of the hydrophobic channels is thus far unknown, but they could provide additional entry/exit routes for O₂ and H₂O₂ to the ferroxidase sites and the core.^{12,19,20}

A crystal structure with Fe(II) present in the active site is difficult to obtain because of the transient nature of substrate/enzyme interactions. However, a number of co-crystals with metal ion homologues for Fe(II) have been achieved that show the di-metal site, e.g. with Mg²⁺²¹ or Ca²⁺²², permitting comparisons with the di-Fe cofactor proteins. As shown in Figure 1, Mg1 in frog M ferritin (top) has a similar ligand motif to that of the Fe(II) in Δ⁹d or R2 (bottom), consisting of two carboxylate and one histidine ligand – E,ExxH.^{18,21} For most diiron proteins this motif is generally repeated at the second iron site, but in ferritin the ligands surrounding the second metal site are substantially different. In the case of the Mg cocrystal with frog M ferritin, selected for study because of the extensive spectroscopic and kinetic characterization that exist,¹² the Mg2 site consists of two glutamates (one is the Glu58 bridge), a glutamine, and an aspartate residue – E,QxxD. Here, the histidine is replaced with a weaker aspartate ligand, and the unusual presence of the glutamine ligand prevents the formation of a second carboxylate bridge between the metals, a structural feature thus far present in all other non-heme diiron sites. These ligands were confirmed in a protein chimera where all M ferritin site Mg ligands (E58, H61, E23, E103, Q137, and D140) were required to confer catalytic activity in a catalytically inactive L ferritin, thus confirming their role in formation of the DFP.¹⁸ The structure of the Fe(II)Fe(II) substrate site in ferritin, including the bridging mode of Glu58, is still unclear.^{21,23}

Despite differences in the active site ligand environments, diferric peroxo intermediates with similar Mössbauer parameters,^{8,14,24-26} absorbance, and resonance Raman features^{9,17,24} have been characterized for ferritin, R2, and Δ⁹d. Although all three peroxo species are thought to have a cis-μ-1,2 structure, quantitative differences in these spectroscopic properties suggest structural differences, particularly among the Fe-O-O angles,^{14,16,17,27-29} which may contribute to their divergent reaction pathways. Decay of the cis-μ-1,2 peroxo observed in R2 leads to a high valent intermediate X,^{11,30} absent in ferritins. In contrast, the DFP in ferritins decays to di-ferric-oxo mineral precursors that are transported from the active site to the mineral cavity of the protein cage.^{13,15}

In order to understand these key differences that exist in the protein-Fe stability and reactivity pathways of ferritins versus cofactor sites (MMO, R2 and Δ⁹d), the geometric and electronic structural features of the Fe(II)Fe(II) site in ferritin must be compared to the other known Fe(II)Fe(II)-protein cofactor sites. A methodology utilizing Circular Dichroism (CD), Magnetic

CD (MCD) and Variable Temperature, Variable Field (VTVH) MCD, which has been developed and applied to biferrous cofactor sites,^{31,32} has been utilized to study the ferroxidase substrate site in M ferritin. CD studies show anaerobic binding of two Fe(II) at the ferritin active site, and demonstrate cooperativity in the binding process. CD/MCD/VTVH MCD define the coordination geometry of each Fe(II) site and the bridging ligation that shows the unique properties of substrate sites relative to cofactor sites. The presence of water ligands, indicated by the CD/MCD data, coupled with the weaker ligand field at Fe2 in this diiron cofactor site, may provide a mechanism for single atom bridge formation in the DFP and release of H₂O₂, as opposed to formation of the high valent intermediate that is observed in some diiron cofactor sites.

Experimental

Sample Preparation

MOPS buffer (Sigma), NaCl (EMD Chemicals, Inc.), deuterium oxide (99.9 atom % D, Aldrich), sodium dithionite (Sigma), dithiothreitol (Sigma), ferrous sulfate heptahydrate (Baker), and glycerol (98% D, Cambridge Isotope Laboratories) were commercially purchased, and used as obtained. Before use in an inert atmosphere, D₂O was degassed with 99.9% pure argon, glycerol was degassed by heating under vacuum overnight at 10⁻³ Torr, and solid ferrous sulfate was put under vacuum at 10⁻³ Torr for at least one hour. Fe(II) stock solutions (~80–120 mM depending on protein concentration), used for reconstitution of the apo-protein, were freshly prepared by adding anaerobic D₂O to a pre-measured amount of degassed solid ferrous sulfate under nitrogen atmosphere before each experiment.

Recombinant apo M ferritin from frog was cloned and expressed in *Escherichia coli*, and purified as previously reported.^{14,33} Adventitious iron trapped in the protein shell (8-20 Fe/ferritin nanocage, as isolated) in the form of a super paramagnetic center exhibits an intense absorption feature that overlaps with and obscures the weaker d-d transitions in the near-IR region that are the focus of this study. Therefore, it was necessary to subject the protein to extensive anaerobic reductive dialysis in the presence of dithiothreitol to ensure all iron was removed from the core and other potential binding sites.³⁴ Dialysis was considered complete when the residual Fe was below the assay detection limit (molar ratio less than 0.1 µg Fe/1 mg Ftn, or less than one Fe per assembled ferritin nanocage).³⁵ The protein buffer solution was then exchanged with a deuterium oxide buffer solution of 100 mM Mops/100 mM NaCl at pD 7.3 until the percentage of D₂O was 99.9% of the solvent. This protein solution was finally concentrated to between 2-8 mM per subunit with one catalytic site/subunit (0.083-0.33mM protein nanocages), and degassed while on ice by rapidly purging with at least 30 vacuum/argon cycles.

To prepare the CD and MCD samples, incremental amounts of Fe(II) stock solution were added to the anaerobic apo-protein solution, and after incubation for ~10 minutes, CD samples were measured in an anaerobic quartz cuvette, which was cooled to 7°C by a recirculating water bath. MCD samples were similarly prepared with an additional step of mixing the protein solution with 50-60% (v/v) glycerol-*d*₆ until homogeneous to create a suitable glass. (From CD studies, the glycerol was found to have no effect on the biferrous site.) The protein samples were then injected into the MCD sample cell (a neoprene spacer of 0.3cm path length compressed between two infrasil quartz disks that are held together between two fitted copper plates) while under an inert atmosphere, and immediately frozen in liquid nitrogen.

CD and MCD Spectroscopy

CD studies were performed on a JASCO J200D spectropolarimeter operating with a liquid nitrogen-cooled InSb detector in the 600-2000 nm region. Low-temperature MCD and VTVH

MCD data were acquired on this spectropolarimeter, modified to accommodate an Oxford Instrument SM4000 7T-superconducting magnet capable of magnetic fields up to 7.0T and temperatures down to 1.5 K. The depolarization of the protein glass was checked by comparing CD spectra taken with a freshly prepared nickel (+)-tartrate solution placed immediately before, and then after the MCD sample compartment.³⁶ Less than ~10% depolarization was observed.

All CD and MCD spectra were baseline corrected by subtracting the apo-protein solution spectrum, or averaging the corresponding positive and negative field spectra at a particular temperature. These spectra were then fit with Gaussian band shapes using a constrained nonlinear least-squares procedure in order to find the minimum number of ligand field transitions required to simultaneously fit both spectra. VTVH MCD data (MCD intensity at a specific wavelength as a function of temperature and applied magnetic field) were fit using a simplex routine that minimizes the χ -squared value. A goodness of fit parameter (χ -squared/number of float parameters) was utilized in the comparison of fit results.

III. Results

A. Metal Binding to the Active Site

Fe(II) binding to the apo-ferritin protein was monitored using Near-IR (NIR) CD and MCD titrations. Addition of Fe(II) produces two positive bands, at 5100 and 10600 cm^{-1} , in the 7°C CD spectrum. In Figure 2 it can be seen that the intensities of these bands increase simultaneously as Fe(II) is added. While fewer titration points can be taken in MCD due to complexity in sample preparation and limitations of the optical glass formed by the sample, low temperature MCD data also show that all MCD features increase together (Figure S1, Supporting Information). At approximately 48 equivalents of iron per ferritin 24mer, where each of the 24 subunits contains a single ferroxidase site (~2 Fe(II) per ferritin ferroxidase site), the band intensities reach a maximum. Further addition of iron under anaerobic conditions does not induce additional change to the CD spectrum and eventually leads to precipitation of the protein; therefore, the substrate sites are fully loaded without adding a stoichiometric excess of iron.

A total of three bands are observed in the 7°C CD spectrum: one low energy transition at 5100 cm^{-1} and two higher energy transitions at 10 075 and 11 450 cm^{-1} , which are resolved from the band at 10 600 cm^{-1} through simultaneous peak fitting of the low temperature CD and MCD data (Section B). A single Fe(II) center can contribute, at most, two transitions in this energy region,³⁷ therefore, two inequivalent Fe(II) centers must contribute to the observed CD spectrum. These Fe(II) centers must be protein bound, as only chiral iron centers will contribute to the CD spectrum.³⁷ To determine Fe(II) binding affinities for the individual iron centers, the CD intensity of each band is plotted against Fe(II) concentration in the inset of Figure 2. The transition at 5100 cm^{-1} is represented by intensity data taken at 5800 cm^{-1} to obtain the largest signal to noise ratio, and the intensities at 9700 and 11 600 cm^{-1} were used for the 10 075 and 11 450 cm^{-1} transitions to minimize their overlap (indicated by the arrows whose colors correspond to the intensity data plotted in the inset of Figure 2). Each transition shows the same binding curve, indicating a concerted rather than independent binding of the Fe(II).

The sigmoidal shapes of these data (Figure 3 and inset of Figure 2) are indicative of cooperative binding, and the relative intensity plot for each transition can be fit to a cooperative binding model using the Hill equation:

$$Y = [\text{Fe}]^n / (K^n + [\text{Fe}]^n) \quad (1)$$

where $K = [\text{P}][\text{Fe}]_n / [\text{P-Fe}_n]$ (P = protein and n = Hill coefficient) and Y = fractional saturation, which is calculated from the CD intensity relative to its saturation value. Using a non-linear

regression method based on the Levenberg-Marquardt (LM) algorithm to minimize chi-squared in Origin,³⁸ each saturation curve is fit with a Hill coefficient, n , of 2.5 - 3.2 (Figure 3, S2). As there is only one binuclear iron site per subunit, but 24 subunits within the ferritin molecule, a Hill coefficient of three must reflect cooperative interactions among a subset of subunits. The data can also be fit in a logarithmic Hill plot (Figure 3 inset, $n \sim 3.3$), which shows that the diiron site must exist in at least two different allosteric states where the binding affinity at the initial state is $K^i \sim 100 \text{ M}^{-1}$, and the affinity in the final state is $K^f \sim 2.3 \times 10^3 \text{ M}^{-1}$. This gives a total allosteric energy ($RT \ln(K^f / K^i)$) for iron binding of $\sim 1.8 \text{ kcal/mol}$.

B. CD and MCD: Gaussian Resolution and Peak assignments

The NIR CD spectrum taken at 7°C , and CD and MCD spectra taken at 1.7K are shown in Figure 4. As determined above, the 7°C CD spectrum shows two large positive bands around 5100 and 10600 cm^{-1} that are unaltered upon the addition of glycerol or increased pH. These peaks sharpen and shift slightly in energy at lower temperature,³⁷ allowing the 1.7K CD spectrum to reveal a negative band around 7600 cm^{-1} flanked by the two positive bands, which overlap in this region of the 7°C CD spectrum to obscure the negative band. The MCD spectrum (Figure 4, bottom), obtained from a sample at a concentration of 90% Fe(II) per ferroxidase site,³⁹ exhibits three distinct bands around 5000 , 7600 , and $10\,000 \text{ cm}^{-1}$, and a resolvable high energy shoulder at $\sim 11\,000 \text{ cm}^{-1}$. A simultaneous fit of the low temperature CD and MCD data gives transitions at 5025 , 7600 , 9900 , and $11\,150 \text{ cm}^{-1}$, resolving the $10,600 \text{ cm}^{-1}$ band of the low temperature CD spectrum into two transitions. These bands result from transitions from the $^5\text{T}_{2g}$ ground state to the doubly degenerate $^5\text{E}_g$ excited state of high spin Fe(II) d^6 centers. In octahedral symmetry, with the nitrogen and oxygen ligands present at the ferroxidase substrate site, these states are split by $10\text{Dq}_{\text{Oh}} \cong 10000 \text{ cm}^{-1}$.⁴⁰ Depending on coordination number and site symmetry, the doubly degenerate $^5\text{E}_g$ excited state for each iron will split, resulting in two d-d transitions at varying energies in the NIR region.^{37,41}

Therefore, the four distinct transitions (Figure 4) in the M ferritin NIR CD/MCD spectra are from the two iron centers of the ferroxidase site, which must have different geometric environments.³⁷ These transitions could be assigned in three possible combinations. First, a 4C Fe(II) could be associated with the transitions at 5025 and 7600 cm^{-1} , requiring transitions at 9900 cm^{-1} and $11\,150 \text{ cm}^{-1}$ to be assigned to a 6C Fe(II). However, the 1250 cm^{-1} splitting of the two high-energy transitions is much smaller than that observed for any 6C model complexes involving a similar ligand set (average splitting $\sim 1800 \text{ cm}^{-1}$),^{31,42,43} and below the 1400 cm^{-1} minimum splitting observed for the excited-state Jahn-Teller distortion of an octahedral $\text{FeSiF}_6 \cdot \text{H}_2\text{O}$ complex.⁴⁰ The two remaining possibilities (assigning the transition at 7600 cm^{-1} with either the $11\,150 \text{ cm}^{-1}$ or 9900 cm^{-1} transition to one iron, with the remaining two bands assigned to the second Fe) both require two inequivalent 5C irons. Analysis of the VTVH MCD saturation data distinguishes between these possibilities and allows specific band assignments and ligand fields to be determined for each iron.

C. VTVH MCD: Ground state analysis

An overlay of the CD and MCD spectra of the two Fe(II) ferroxidase site in M ferritin is shown in Figure 5A. Increasing field or decreasing temperature leads to an increase, and eventual saturation, of the MCD intensity of all four transitions (Figure S4, supplementary information), indicating that each is dominated by an MCD C-term mechanism associated with a paramagnetic doublet ground-state. By taking VTVH MCD data at different energies, different saturation rates and behaviors are observed, reflecting the Fe(II) center and polarization associated with that transition.³⁷ Therefore, VTVH MCD data were collected at energies where there is minimal overlap of resolved band intensities. In M ferritin, VTVH MCD data were obtained at 5025 , 7600 , and 9900 cm^{-1} (positions indicated by the arrows in Figure 5A), and are shown in Figure 5B-D, where the relative intensities of the VTVH MCD curves are plotted

against $\beta H/2kT$. Acceptable VTVH data could not be collected on the transition at 11 150 cm^{-1} , due to low signal intensity and overlap with the band at 9900 cm^{-1} .

The offset of the low temperature isotherms from those at higher temperatures (Figure 5B-D) is characteristic of low lying excited states and rhombic zero-field splitting (ZFS) of non-Kramers doublet ground states. These splittings reflect the ZFS parameters (D , E) of each Fe (II) and the exchange coupling between the irons (J) associated with the bridging ligands.⁴⁴ While most non-Kramers systems lack an EPR signal, ground state parameters can be obtained through doublet fitting of the VTVH MCD intensity (Figure 5).^{31,37} This model includes the contribution of the second-order Zeeman effect as a linear B-term resulting from the field induced mixing between different doublet states and determines the g_{\parallel} (the Zeeman splitting of the non-Kramers doublet) and δ (the rhombic ZFS of the doublet in the absence of a magnetic field) for the ground state and low lying sublevels. These values can be used as a starting point for a spin-projection model. This model calculates the MCD intensity directly from the dimer wave functions using the fact that this intensity is directly proportional to the spin expectation values of the iron center associated with the LF transition projected onto the dimer states.⁴⁵ Thus, the Fe(II) center associated with a particular transition can often be determined by its ZFS. The combined analyses of these data generate a description of the ground-state electronic structure of the reduced ferroxidase site in M ferritin.

1. Doublet Model—The VTVH MCD data in Figure 5 were first fit using equation 2 that has been derived for non-Kramers systems:^{37,46,47}

$$\Delta\varepsilon = \sum_i \left[(A_{\text{satlim}})_i \left(\int_0^{\frac{\pi}{2}} \frac{\cos^2 \theta \sin \theta}{\Gamma_i} g_{\parallel i} \beta H \alpha_i d\theta - \sqrt{2} \frac{M_z}{M_{xy}} \int_0^{\frac{\pi}{2}} \frac{\sin^3 \theta}{\Gamma_i} g_{\perp i} \beta H \alpha_i d\theta \right) + B_i H \gamma_i \right] \quad (2)$$

where

$$\begin{aligned} \Gamma_i &= \sqrt{\delta_i^2 + (g_{\parallel i} \beta H \cos \theta)^2 + (g_{\perp i} \beta H \sin \theta)^2} \\ \alpha_i &= \frac{e^{-(E_i - \Gamma_i/2)/kT} - e^{-(E_i + \Gamma_i/2)/kT}}{\sum_j e^{-(E_j - \Gamma_j/2)/kT} + e^{-(E_j + \Gamma_j/2)/kT}} \\ \gamma_i &= \frac{e^{-(E_i - \delta_i/2)/kT} + e^{-(E_i + \delta_i/2)/kT}}{\sum_j e^{-(E_j - \beta_j/2)/kT} + e^{-(E_j + \delta_j/2)/kT}} \end{aligned}$$

This equation allows for the contribution of C-term intensity, $(A_{\text{satlim}})_i$, the rhombic ZFS for a non-Kramers doublet, δ_i , the effects of a linear B-term from field induced mixing between states, B_i , and the presence of thermally excited sublevels of the ground state. E_i is the energy of the i^{th} excited state, and the energy of the ground state is defined as zero. The Boltzmann population over all states has been included in both the C- term and the B- term intensities as the factors α_i and γ_i , respectively. H is the applied magnetic field, k the Boltzmann constant, M_z and M_{xy} are the transition dipole moments for the directions indicated, and $g_{\parallel i}$ and $g_{\perp i}$ are the Zeeman splitting parameters of the i th doublet.

The lowest temperature isotherm of each VTVH MCD data set was fit with equation 2 by fixing g_{\parallel} to values associated with each of the possible ground states for a high spin Fe(II) dimer system (0, 4, 8, 12, and 16), while floating $(A_{\text{satlim}})_0$, B_0 , and δ_0 . M_z/M_{xy} and $g_{\perp i}$ were initially fixed at zero. Fits to the first isotherm were evaluated based upon minimization of χ^2 , a goodness of fit parameter, and through visual examination of the fit to be within standard

deviation of the plotted data. Once a best fit was obtained, g_{\parallel} , M_z/M_{xy} , and $g_{\perp i}$ were allowed to float; however, this did not significantly alter the fit. The signal to noise ratio of the data taken at 5025 cm^{-1} was fairly large and could only rule out g_{\parallel} of 0, 4, and 16, however, good fits for VTVH data at 7600 and 9900 cm^{-1} were independently achieved with $g_{\parallel} \sim 8$ and $\delta_0 \sim 4.3 \text{ cm}^{-1}$, indicative of a $M_s = \pm 2$ ground state. Differences in the $(A_{\text{satlim}})_0$ and B_0 parameters account for the significantly different saturation behaviors of each transition. These reflect the different Fe(II) centers associated with each transition studied.

At approximately 10K, a low-lying excited state began to populate requiring the inclusion of an excited doublet state to achieve an acceptable fit to the data. For this Fe(II)Fe(II) coupled system, the first possible excited state can have $M_s = \pm 1$ or $M_s = \pm 3$ (as obtained from the spin-Hamiltonian analysis in the following section). Best fits to all three data sets, in agreement with the spin-Hamiltonian analysis below, were obtained with a low-lying excited state at 3.4 cm^{-1} above the ground state having an $M_s = \pm 1$, associated with a $g_{\parallel} \sim 4$. As shown in Figure 5B-D, the calculated curves for all isotherms were now within the standard deviation of the averaged data points; therefore, additional excited states could not be determined. Final fit parameters are given in Table 1. The fact that the fits to the VTVH MCD data from each transition require the same dimer spin state energy level diagram is consistent with these transitions resulting from an exchange coupled dimer system. This assignment is confirmed through a full spin-Hamiltonian analysis (*vide infra*) that directly considers the ground state of a spin-coupled system.

2. Spin-Hamiltonian Analysis—A high-spin ferrous ion has an $S = 2$ ground state that is 5-fold degenerate in $M_s = 0, \pm 1$, and ± 2 . These will split in energy due to ZFS, given by the parameters D (axial) and E (rhombic). In a bridged diiron system, the two ferrous centers interact to form exchange coupled dimer states with $S_{\text{tot}} = |S_1 + S_2| \dots |S_1 - S_2| = 4, 3, 2, 1$ and 0 . These levels are split in energy by the exchange coupling $H = -2JS_1S_2$ to generate $(2S_{\text{tot}} + 1) M_{S_{\text{tot}}}$ degenerate levels. In binuclear non-heme ferrous systems, the magnitude of the exchange coupling, J , is comparable to its zero field splitting, D , therefore, both effects must be simultaneously considered.⁴⁸ This is accomplished through the spin Hamiltonian given by equation 3, which operates on the uncoupled basis set $|S_1, S_2, M_{s1}, M_{s2}\rangle$, where the subscripts indicate the two ferrous centers.^{32,48-50}

$$H = -2J\hat{S}_1 \cdot \hat{S}_2 + D_1(\hat{S}_{z1}^2 - 1/3S(S+1)) + E_1(\hat{S}_{x1}^2 - \hat{S}_{y1}^2) + D_2(\hat{S}_{z2}^2 - 1/3S(S+1)) + E_2(\hat{S}_{x2}^2 - \hat{S}_{y2}^2) + g_{z1}\beta H_z S_{z1} + g_{x1}\beta H_x S_{x1} + g_{y1}\beta H_y S_{y1} + g_{z2}\beta H_z S_{z2} + g_{x2}\beta H_x S_{x2} + g_{y2}\beta H_y S_{y2} \quad (3)$$

Zeeman terms ($g_{z1}\beta H_z S_{z1} \dots$ etc.) are also included, where the g value can be coupled to the ZFS parameters using ligand field theory as given in Equations 2a and 2b. k^2 is the Stevens orbital reduction factor, i.e. ($|k| < 1$), and accounts for the effects of covalency, and is λ the Fe (II) ground state spin-orbit coupling constant ($\sim 100 \text{ cm}^{-1}$).

$$D_{\text{Fe}^{2+}} = \frac{-k^2\lambda}{4} (g_{x\text{Fe}^{2+}} + g_{y\text{Fe}^{2+}} - 2g_{z\text{Fe}^{2+}}) \quad (3a)$$

$$E_{\text{Fe}^{2+}} = \frac{-k^2\lambda}{4} (g_{y\text{Fe}^{2+}} - g_{x\text{Fe}^{2+}}) \quad (3b)$$

Application of this spin-Hamiltonian to the uncoupled basis set generates a 25×25 matrix, which is diagonalized to determine the wave functions of these binuclear ferrous spin states and their relative energies. The zero field splitting, D , is constrained to be less than $|15 \text{ cm}^{-1}|$, the largest value observed in model systems and ligand field calculations, and $|E/D|$ must be

$\leq 1/3$ by definition. The resultant energies and order of these spin states are dependent on the relative signs and magnitudes of J and D . The $M_s = \pm 2$ ground state, determined for this system by the doublet analysis, can only be generated if the two irons have D -values with opposite signs.³²

Figure 6A presents the energy level diagram generated with $D_1 = -9.9 \text{ cm}^{-1}$, $D_2 = +4.6 \text{ cm}^{-1}$, and E/D ratios of 0 for both irons, for a range of J values from -5 to 5 . However, fits using the doublet model required a large δ_0 to reproduce the nesting behavior of the VTVH data, indicating that there must be a rhombic splitting of the ground state.³⁷ Increasing the rhombicity of each iron removes all degeneracy of the doublet spin states and mixes the wave functions (Supplemental Figure S5 A). Near the rhombic limit, at $E/D > 0.25$ and $-1 < \sim J < 0$, the sublevels of the doublets become embedded, resulting in alternating states of $M_s = \pm 2$ and $M_s = \pm 1$, as shown in the energy level diagram in Figure 6B, generated with $D_1 = -9.9 \text{ cm}^{-1}$ and $D_2 = +4.6 \text{ cm}^{-1}$ and E/D ratios of 0.3 for each iron. Upon application of a magnetic field, the ground and excited state doublets studied show splitting behavior characteristic of a $g = 8$ and $g = 4$ respectively (Supplemental Figure S5 B-C), even after the sublevels of the doublets cross (Figure 6B and S5D). Therefore, although there are differences in energy splitting due to mixing, the energy diagram for a rhombic system can still be modeled by a set of doublet spin states.

From these diagrams (Figure 6), it can be seen that a ground state of $M_s = \pm 2$ is only possible for systems with weak exchange coupling, $-1 < \sim J < 1 \text{ cm}^{-1}$. Therefore, the M_s value of the first excited doublet determines the sign of J . For a ferromagnetic system, the first excited state is $M_s = \pm 3$, while for an anti-ferromagnetic system the first excited state is $M_s = \pm 1$. As this excited doublet state was determined to have $g_{\parallel} = 4$ (table 1) corresponding with an $M_s = \pm 1$, the binuclear Fe(II) active site of M ferritin must be weakly anti-ferromagnetically coupled, with $0 > J > -1 \text{ cm}^{-1}$.

3. Spin-Projection Model—The different saturation magnetization behaviors of the data in Figures 5B-D have thus far been accounted for through the inclusion of empirical C-term ($A_{\text{satlim}})_i$ and B-term contributions to MCD intensity. A complementary fitting approach of these VTVH MCD data was also performed by relating the different saturation magnetization behaviors of the MCD transitions to differences in the spin expectation values of the iron being studied, using the dimer wave functions given by the Hamiltonian in equation 3. The MCD intensity is proportional to the spin expectation value of a sublevel in the direction perpendicular to the two transition polarizations giving MCD intensity, averaged over all molecular orientations (equation 4).^{32,45}

$$\frac{\Delta\epsilon}{E} = \frac{\gamma}{4\pi S} \int_0^{\pi} \int_0^{2\pi} \sum_i N_i \left(l_x \langle S_{1,x} \rangle_i M_{yz}^{\text{eff}} + l_y \langle S_{1,y} \rangle_i M_{xz}^{\text{eff}} + l_z \langle S_{1,z} \rangle_i M_{xy}^{\text{eff}} \right) \sin\theta d\theta d\varphi \quad (4)$$

Here, $\Delta\epsilon/E$ is the MCD intensity, the l 's are direction cosines, θ is the angle of the magnetic field and the molecular z -axis, φ is the angle of the xy -projection of the magnetic field with the molecular y -axis, the M_{ij} 's are effective transition dipole moment products for two perpendicular polarizations ($i \neq j$) that account for differences in nesting behavior, and $\langle S_{1,p} \rangle_i$ is the p 'th component (perpendicular to i and j) of the spin-expectation value of the i 'th ground state sublevel localized on Fe1. Numeric simulations and least squares fits of VTVH MCD data to equation 4 yield the ground state magnetic coupling parameters J , D_1 , E_1 , D_2 , and E_2 , with Fe₁ being the center associated with the ligand field transition used to obtain the saturation magnetization data.

As determined from the doublet model and spin-Hamiltonian analysis, to achieve a $g_{\parallel} \sim 8$ ground state in a coupled binuclear system, the two ZFS D -values must be of opposite signs.

For a single Fe center, the sign of D would not affect such a rhombic system. In a dimer, however, different energy splitting patterns for different directions of the applied magnetic field will result from the relative orientation of the D tensors of the two iron centers, which are dependent on the sign of D. Therefore the polarization of a transition from one Fe center may have a different affect on the saturation behavior, depending on its individual axes system. Fits to the VTVH MCD data taken at 7600 cm^{-1} were calculated with starting D_1 values of $\pm 5\text{ cm}^{-1}$ and $\pm 10\text{ cm}^{-1}$, and anti-ferromagnetic J values between 0.0 and -1.0. From this analysis, it was determined that the transition at 7600 cm^{-1} is mostly x-polarized and the associated Fe (II) has a ZFS of $+4.6\text{ cm}^{-1}$ and $E/D \sim 0.3$. A -J of $\sim 0.8\text{ cm}^{-1}$ was determined for the dimer (Figure 6 and Supplemental Figure S6). A best fit to the VTVH data taken at 9900 cm^{-1} was obtained with a D of -9.75 cm^{-1} , $E/D \sim 0.3$, and $-J \sim 0.9\text{ cm}^{-1}$ (Figure S7). The large E/D ratios of ~ 0.3 assigned to both Fe centers are consistent with the large δ of $\sim 4\text{ cm}^{-1}$ determined for the ground state of this system using the doublet model fitting. The standard deviation on the data taken at 5025 cm^{-1} is fairly large, as this is near the limit of the detector and in a region where D_2O from the buffer begins to absorb, preventing a rigorous fit of these data. A visual comparison of the fits, however, does support a D of $\sim -10.0\text{ cm}^{-1}$ for the Fe(II) associated with this band (Figure S8). The spin-projection fitting parameters are summarized in Table 2.

The assignment of D-values to three of the four transitions distinguishes the two iron environments. Transitions at 9900 and $11\,150\text{ cm}^{-1}$ cannot be assigned to the same iron due to their small energy splitting.⁴⁰ The remaining assignments could pair the transition at 7600 cm^{-1} with either the 9900 and $11\,150\text{ cm}^{-1}$ transition. The spin-projection analysis determined that the bands at 7600 and 9900 cm^{-1} have oppositely signed D's requiring these transitions to be assigned to different Fe(II) centers. Thus the bands at 7600 cm^{-1} and $11\,150\text{ cm}^{-1}$ must derive from a single Fe(II) center. The smaller positive D-value and high energy transition $>10\,000\text{ cm}^{-1}$ associated with this iron are indicative of a distorted square pyramidal geometry with a strong axial ligand.³⁷ This requires the bands at 5025 and 9900 cm^{-1} be assigned to the second Fe(II) center, having a negative D-value and transitions $<10\,000\text{ cm}^{-1}$, consistent with a trigonal bipyramidal geometry.³⁷

Discussion

The combination of CD, MCD, and VTVH MCD spectroscopies has been applied to Fe(II) binding at the diiron substrate site of M ferritin, the first ferritin protein studied by this methodology, to gain geometric and electronic insights for comparison to diiron cofactor sites. In the spectrum of the biferrous substrate site, the set of MCD transitions at 7600 and $11\,150\text{ cm}^{-1}$ exhibit a much smaller excited state splitting ($\sim 3550\text{ cm}^{-1}$) than typical for 5C iron centers ($\sim 5000\text{ cm}^{-1}$). A similar energy splitting ($\sim 3000\text{ cm}^{-1}$) observed for the 5C irons in $\Delta^9\text{d}$ had been attributed to the terminal glutamate ligands binding in a bidentate fashion to the Fe(II), distorting the square pyramidal geometry.¹ The glu23, glu58, and his61 ligands at the Fe1 center in the ferritin substrate site, where Fe1 corresponds to Mg1 in the crystal structure (Figure 1),^{18,21} provide a similar environment allowing the first set of transitions to be assigned to this Fe(II) center. The ligand field of the Fe2 center corresponds to Mg2 in Figure 1 and is much weaker than any previously observed Fe(II) centers due to the gln137 and asp140 ligands.^{18,21} This results in two LF transitions at lower energies than those of Fe1, consistent with correlation of the second set of transitions at 5025 and 9900 cm^{-1} to Fe2. Each site provides only four amino acid ligands to the bound Fe(II) substrates in ferritin. Bidentate coordination to Fe2 by the terminal Glu103 and Asp140 ligands would be prevented by hydrogen bonding interactions, and Gln137 cannot form a bridge to Fe1. Therefore, water molecules must account for the additional ligand on each of the 5C Fe(II) centers described by MCD. A stronger axial histidine-Fe interaction would compensate for the weaker water ligand on Fe1, leading to the positive ZFS observed for the iron associated these transitions, while the weaker axial ligands available at Fe2 are more consistent with the negative ZFS associated with this iron center.

Two possible water coordination schemes for the diferrous substrate site in ferritin were evaluated by VTVH MCD: a single water-derived ligand bridging the site or individual waters bound to each Fe(II). A μ -aquo bridge in a biferrous site appears to result in ferromagnetic coupling,^{51,52} while a hydroxide bridge has been associated with strong anti-ferromagnetic coupling ($-J \sim 14\text{cm}^{-1}$) for biferrous systems.⁵³ In ferritin, however, the two substrate Fe(II) ions are very weakly anti-ferromagnetically coupled ($-J \sim 0.8\text{cm}^{-1}$), indicating that there are no water derived ligand bridges at the Fe(II)Fe(II) site. The weak coupling is, however, consistent with a μ -1,3 bridging orientation for the Glu58 ligand. A model for two Fe(II) substrate ions bound at the ferroxidase site is shown in scheme 1 (top left) with the water on Fe1 hydrogen bonded to Gln137 and the water bound to Fe2 opposite Glu103.

All CD and MCD transitions (Figure 2,S1) associated with this ferroxidase site saturate simultaneously during titration with Fe(II), supporting a model of concerted binding of the two Fe(II) to the active site (i.e. any occupied ferroxidase site is loaded with two Fe(II) at equilibrium). Comparison of crystal structures with apo and Zn(II) loaded active sites shows that in the Zn-occupied structure the bridging glutamate rotates approximately 55° , facilitating a μ -1,3 bridging orientation between the metals, and the Zn2 glutamine ligand forms a hydrogen bond to the water ligand on Zn1.^{22,54} These structural changes upon Fe1 binding could increase the affinity of the Fe2 site, and therefore lead to concerted binding of the second Fe (II) to form a complete ferroxidase site. Studies of Fe(II) binding to human H ferritin suggested a preferential Fe(II) binding at the Fe1 site with the addition of O_2 necessary for the second Fe to bind.^{55,56} The non-binding alanine residue at the Fe2 site in H ferritin, replacing Asp140 in the M site, could account for this difference in Fe (II) binding, but differences could also relate to the indirect analytical methods used, 1,10-phenanthroline competition for Fe at di-Fe substrate sites, or isothermal calorimetry, compared to the direct monitoring of the active site used in this study. For M ferritin, a partially loaded site would have exhibited different ratios of MCD transition intensities or different temperature and field dependent saturation behavior at different Fe(II) concentrations. The lack of these features supports the presence of biferrous sites at all levels of iron loading in the absence of oxygen.

Positive cooperativity between fully formed substrate sites was observed during Fe(II) binding (Figure 3, S2). The cooperativity cannot relate to sequential Fe(II) binding, since the same cooperativity was observed for transitions associated with both the Fe1 and Fe2 sites, nor to O_2 binding, since O_2 was absent from the reaction. Thus as Fe(II) concentration increased, subunit interactions likely caused the diiron substrate site to shift from a low to a high affinity state. Solvent chains linking the substrate site with the channels formed by three subunits were observed in ferritin protein crystals.²⁰ Such interactions between subunits surrounding the hydrophobic and hydrophilic channels may thus provide a mechanism for allosteric control of substrate entry/exit, and would be consistent with the observed Hill coefficient ($n \sim 3$). The parallel formation of Fe(III) oxo/hydroxo cluster ($\sim 8\text{--}12\text{ Fe}/\text{cluster}$) products from the decay and release of the diferric peroxo intermediate,¹⁵ support the conclusion of active site cooperativity during product release. Cooperativity among the multiple ferrous/dioxygen oxidoreductase sites in ferritin could increase the rate of Fe(II) and O_2 substrate binding during multiple turnovers and increase the nuclearity of mineral precursors. Establishment of a ferric mineral core and higher Fe(II) influx to the protein allow the ferritin molecule to utilize Fe(II) + H_2O_2 detoxification pathways not available to low iron systems,¹³ thus more efficient loading and faster core formation may also allow for a decrease in the release of H_2O_2 .

Characterization of the diiron sites in ferritin and other cofactor diiron enzymes by CD/MCD, Mössbauer, UV-vis, and resonance Raman spectroscopies, has revealed important similarities and differences in the geometric and electronic structures of substrate versus cofactor sites. The Fe(II)Fe(II) active sites in ferritin, R2, and $\Delta^9\text{d}$ +substrate all exhibit weak anti-ferromagnetic coupling consistent with μ -1,3 carboxylate bridges, in contrast to the

ferromagnetic coupling and $g_{\parallel} = 16$ ground state of the MmoH+MmoB active site, associated with a μ -1,1 carboxylate bridge (Table 3). The presence of a single carboxylate bridge in the ferritin substrate site, however, distinguishes it from all cofactor sites, which contain two carboxylate bridges. A conserved glutamine residue in the ferritin substrate site prevents the formation of a second bridge. Since carboxylate bridges do not provide efficient super-exchange pathways for electron transfer, O_2 must bridge the two Fe(II) ions at the active site for energetically favorable two electron reduction.^{4,57} In all these biferrous enzymes, each Fe site is coordinatively unsaturated, leaving at least one vacant position available for dioxygen to bind and form a bridged peroxo intermediate.

The absence of a second carboxylate bridge in the ferritin active site may contribute to the short Fe-Fe distance in the ferritin DFP suggested by quantitative differences in the Mössbauer, absorbance and resonance Raman features (Table 3). The ferritin DFP has a lower $\nu(O-O)$ coupled with a higher $\nu(Fe-O)$, indicating a decrease in the Fe-O-O angle^{17,29} relative to the peroxo intermediate in R2,⁵⁸ consistent with the short Fe-Fe distance determined by EXAFS (2.53Å).¹⁶ A similarly short metal-metal distance also occurs in a triply bridged binuclear Mn (IV) model complex, and was proposed for the DFP structure in ferritin¹⁶ (scheme 1, left). The availability of water ligands, coupled with the presence of an open bridging position at the ferroxidase site, provide a mechanism for single atom bridge formation not available in Δ^9d or R2, supporting the short Fe-Fe distance that would promote release of hydrogen peroxide.^{13,15}

One or both of the water ligands in the ferritin substrate site may form aquo or hydroxo bridges in the peroxo species. The smaller ΔE_Q ^{14,59} and relatively weak exchange coupling ($-J = 37.5 \pm 5 \text{ cm}^{-1}$ with $H = -2JS_1 \cdot S_2$)⁶⁰ between the ferric centers of the DFP rule out the possibility of an oxo bridge.⁵⁹ Rearrangement of the terminal and bridging glutamate ligands, shown to have a relatively small energy barrier,⁶¹ may open an additional coordination position or create a second single atom bridge. Since oxidation of the Fe centers decreases the pK_a of bound water, the water-derived bridge(s) of the peroxo intermediate and the second water coordinated to Fe(III) may then provide the protons necessary for loss of hydrogen peroxide. This would result in oxo or hydroxo bridged diferric species, both of which have been observed as decay products of the peroxo intermediate.^{15,27,62,63} In the cofactor enzymes Δ^9d and R2, there is no coordinated proton source within the biferrous active site to bridge or react with their peroxo intermediates, which undergo alternate decay pathways.³²

In summary, the key differences between the diferrous substrates in ferritin and the diferrous cofactor sites in MmoH, R2 and Δ^9d are: 1) the single glutamate bridge between the bound Fe (II) atoms, 2) two water ligands, one coordinated to each Fe(II), 3) the weaker ligand field, and 4) the concerted Fe(II) binding mechanism and cooperativity. It has not yet been determined whether the inter-subunit cooperativity of biferrous binding to ferritin substrate sites is simply a consequence of multiple sites, or another distinctive property of ferritin catalysis. However, the ferritin-specific, single glutamate bridge of the biferrous substrate site, the proton source from the waters coordinated to each Fe atom, and the weaker ligand field are significant factors in determining the transient nature of the Fe-protein interactions at the ferroxidase site and the release of the diferric-oxo/hydroxo products that form the hydrated ferric oxide mineral.

Supplementary Material

Refer to Web version on PubMed Central for supplementary material.

Acknowledgements

Financial support for this research by NSF-Biophysics Program Grant MCB-0342807 (E.I.S.), NIH Hematology Program DK20251 (E.C.T, X.S.L., T.T), Coollet's Anemia Foundation (X.S.L), and JSPS fellowship for research abroad (T.T).

References

1. Yang YS, Broadwater JA, Pulver SC, Fox BG, Solomon EI. *J Am Chem Soc* 1999;121:2770–2783.
2. Pulver S, Froland WA, Fox BG, Lipscomb JD, Solomon EI. *J Am Chem Soc* 1993;115:12409–12422.
3. Wei PP, Skulan AJ, Mitic N, Yang YS, Saleh L, Bollinger JM, Solomon EI. *J Am Chem Soc* 2004;126:3777–3788. [PubMed: 15038731]
4. Yang YS, Baldwin J, Ley BA, Bollinger JM Jr, Solomon EI. *J Am Chem Soc* 2000;122:8495–8510.
5. Whittington DA, Lippard SJ. *J Am Chem Soc* 2001;123:827–838. [PubMed: 11456616]
6. Lindqvist Y, Huang W, Schneider G, Shanklin J. *Embo J* 1996;15:4081–4092. [PubMed: 8861937]
7. Logan D, Su X, Aberg A, Regnstrom K, Hajdu J, Eklund H, Nordlund P. *Structure* 1996;4:1053–1064. [PubMed: 8805591]
8. Bollinger JM Jr, Krebs C, Vicol A, Chen S, Ley BA, Edmondson DE, Huynh BH. *J Am Chem Soc* 1998;120:1094–1095.
9. Broadwater JA, Ai JY, Loehr TM, Sanders-Loehr J, Fox BG. *Biochemistry* 1998;37:14664–14671. [PubMed: 9778341]
10. Lee SK, Nesheim JC, Lipscomb JD. *J Biol Chem* 1993;268:21569–21577. [PubMed: 8408008]
11. Mitic N, Clay MD, Saleh L, Bollinger JM Jr, Solomon EI. *J Am Chem Soc* 2007;129:9049–9065. [PubMed: 17602477]
12. Liu X, Theil EC. *Acc Chem Res* 2005;38:167–175. [PubMed: 15766235]
13. Zhao G, Bou-Abdallah F, Arosio P, Levi S, Janus-Chandler C, Chasteen ND. *Biochemistry* 2003;42:3142–3150. [PubMed: 12627982]
14. Pereira AS, Small W, Krebs C, Tavares P, Edmondson DE, Theil EC, Huynh BH. *Biochemistry* 1998;37:9871–9876. [PubMed: 9665690]
15. Jameson GNL, Jin W, Krebs C, Perreira AS, Tavares P, Liu X, Theil EC, Huynh BH. *Biochemistry* 2002;41:13435–13443. [PubMed: 12416989]
16. Hwang J, Krebs C, Huynh BH, Edmondson DE, Theil EC, Pennerhahn JE. *Science* 2000;287:122–125. [PubMed: 10615044]
17. Moenne-Loccoz P, Krebs C, Herlihy K, Edmondson DE, Theil EC, Huynh BH, Loehr TM. *Biochemistry* 1999;38:5290–5295. [PubMed: 10220314]
18. Liu X, Theil EC. *Proc Nat Acad USA* 2004;101:8557–8562.
19. Lewin AC, Moore GR, Le Brun NE. *Dalton Trans* 2005;21:3597–3610. [PubMed: 16258608]
20. Trikha J, Theil EC, Allewell NM. *J Mol Biol* 1995;248:949–967. [PubMed: 7760335]
21. Ha Y, Shi D, Small GW, Theil EC, Allewell NM. *J Biol Inorg Chem* 1999;4:243–256. [PubMed: 10439069]
22. Hempstead PD, Yewdall SJ, Fernie AR, Lawson DM, Artymiuk PJ, Rice DW, Ford GC, Harrison PM. *J Mol Biol* 1997;268:424–448. [PubMed: 9159481]
23. Bacelo DE, Binning RC Jr. *Inorg Chem* 2006;45:10263–10269. [PubMed: 17140234]
24. Moenne-Loccoz P, Baldwin J, Ley BA, Loehr TM, Bollinger JM. *Biochemistry* 1998;37:14659–14663. [PubMed: 9778340]
25. Broadwater JA, Achim C, Münck E, Fox BG. *Biochemistry* 1999;38:12197–12204. [PubMed: 10493786]
26. Kauffmann K, Popescu CV, Dong Y, Lipscomb JD, Que L, Munck E. *J Am Chem Soc* 1998;120:8739–8746.
27. Krebs C, Edmondson DE, Huynh BH. *Methods Enzymol* 2002;354:436–454. [PubMed: 12418245]
28. Bou-Abdallah F, Papaefthymiou GC, Scheswohl DM, Stanga SD, Arosio P, Chasteen ND. *Biochem J* 2002;364:57–63. [PubMed: 11988076]

29. Brunold TC, Tamura N, Kitajima N, Morooka Y, Solomon EI. *J Am Chem Soc* 1998;120:5674–5690.
30. Burdi D, Willems JP, RiggsGelasco P, Antholine WE, Stubbe J, Hoffman BM. *J Am Chem Soc* 1998;120:12910–12919.
31. Pavel E, Kitajima N, Solomon E. *J Am Chem Soc* 1998;120:3949–3962.
32. Solomon EI, Brunold TC, Davis MI, Kemsley JN, Lee SK, Lehnert N, Neese F, Skulan AJ, Yang YS, Zhou J. *Chem Rev* 2000;100:235–349. [PubMed: 11749238]
33. Waldo GS, Theil EC. *Biochemistry* 1993;32:13262–13269. [PubMed: 8241182]
34. Treffry A, Hirzmann J, Yewdall SJ, Harrison PM. *FEBS* 1992;302:108–112.
35. Michaelis L, Granick S. *J Biol Chem* 1943;147:91–97.
36. Browett WR, Fucaloro AF, Morgan TV, Stephens PJ. *J Am Chem Soc* 1983;105:1868–1872.
37. Solomon EI, Pavel EG, Loeb KE, Campochiaro C. *Coord Chem Rev* 1995;144:369–460.
38. Microcal Software, I.; NorthHampton, MA: 1991. <http://www.microcal.com>
39. The MCD of aqueous Fe(II) (Figure S3) would overlap the higher energy MCD features of the ferroxidase site if excess Fe(II) were present. However, the CD intensity saturates at approximately two equivalents of Fe(II)/binuclear site (Figure 2), indicating a strong binding affinity, therefore, very little aqueous Fe(II) will be present if less than two equivalents of Fe(II) are added. Additionally, the presence of these high energy MCD features in the CD require that these transitions derive from chiral, protein bound species (Solomon EI, Pavel EG, Loeb KE, Campochiaro C. *Coord Chem Rev* 1995;144:369–460.).
40. Jones GD. *Phys Rev* 1967;155:259–261.
41. Pavel EG, Martins LJ, Ellis WR Jr, Solomon EI. *Chem Biol* 1994;1:173–183. [PubMed: 9383387]
42. Liehr AD, Ballhausen CJ. *Annals of Physics* 1958;3:304–319.
43. Cotton FA, Meyers MD. *J Am Chem Soc* 1960;82:5023–5026.
44. Zhang Y, Gebhard MS, Solomon EI. *J Am Chem Soc* 1991;113:5162–5175.
45. Neese F, Solomon EI. *Inorg Chem* 1999;38:1847–1865. [PubMed: 11670957]
46. Stevens PJ. *Ann Rev Phys Chem* 1974;25:201.
47. Bennet DE, Johnson MK. *Biophys Acta* 1987;911:71–80.
48. Kahn, O. *Molecular Magnetism*. VCH Publishers, Inc.; New York: 1993.
49. Bencini, A.; Gatteschi, D. *Inorganic Electronic Structure and Spectroscopy*. Solomon, EI.; Lever, ABP., editors. 1. John Wiley & Sons; New York: 1999. p. 93-160.
50. Moriya T. *Phys Rev* 1960;120:91–98.
51. Reem RC, Solomon EI. *J Am Chem Soc* 1987;109:1216–1226.
52. Hagen KS, Lachicotte R. *J Am Chem Soc* 1992;114:8741–8742.
53. Brunold TC, Solomon EI. *J Am Chem Soc* 1999;121:8277–8287.
54. Toussaint L, Bertrand L, Hue L, Crichton RR, Declercq JP. *J Mol Biol* 2007;365:440–452. [PubMed: 17070541]
55. Bou-Abdallah F, Arosio P, Santambrogio P, Yang X, Janus-Chandler C, Chasteen ND. *Biochemistry* 2002;41:11184–11191. [PubMed: 12220183]
56. Treffry A, Zhao Z, Quail MA, Guest JR, Harrison PM. *Biochemistry* 1997;36:432–441. [PubMed: 9003196]
57. Wei P, Skulan AJ, Wade H, DeGrado WF, Solomon EI. *J Am Chem Soc* 2005;127:16098–16106. [PubMed: 16287296]
58. Skulan AJ, Brunold TC, Baldwin J, Saleh L, Bollinger JM, Solomon EI. *J Am Chem Soc* 2004;126:8842–8855. [PubMed: 15250738]
59. Kurtz D. *Chem Rev* 1990;90:585–606.
60. Krebs C, Bollinger J, Theil E, Huynh B. *J Biol Inorg Chem* 2002;7:863–869. [PubMed: 12203023]
61. Torrent M, Musaev D, Morokuma K. *J Phys Chem B* 2001;105:322–327.
62. Bauminger ER, Harrison PM. *Hyperfine Interact* 2003;151:3–19.
63. Pereira AS, Tavares P, Lloyd SG, Danger D, Edmondson DE, Theil EC, Huynh BH. *Biochemistry* 1997;36:7917–7927. [PubMed: 9201937]

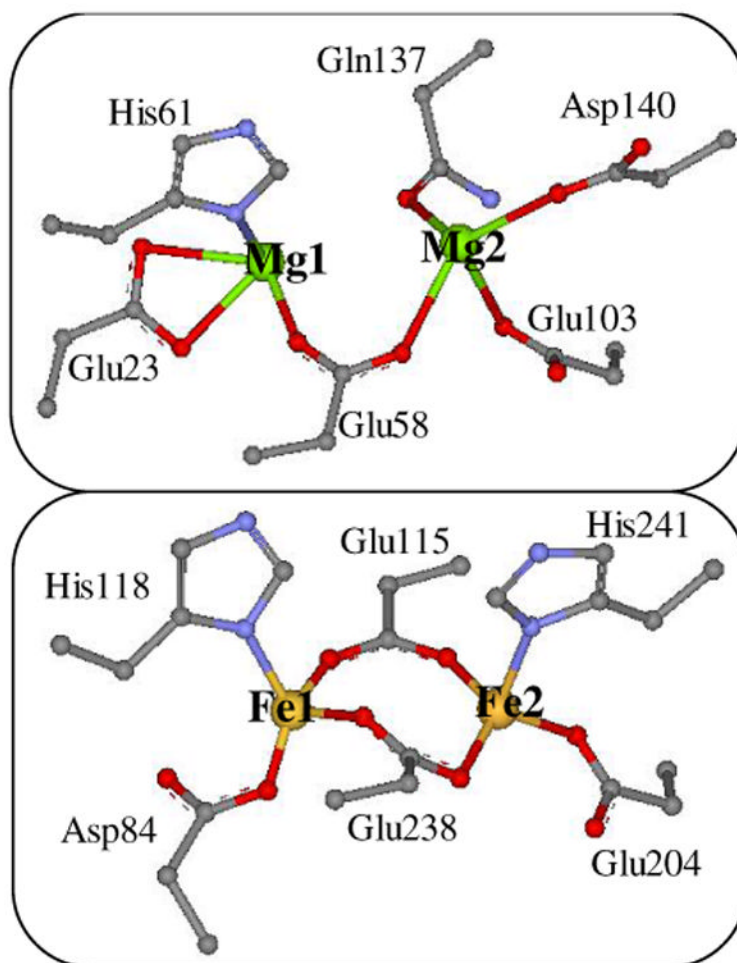


Figure 1.

Crystal structures of the active sites in (top) M ferritin (1mfr) crystallized with Mg(II) and (bottom) Ribonucleotide Reductase from *E. coli* (1XIK) crystallized with Fe(II)

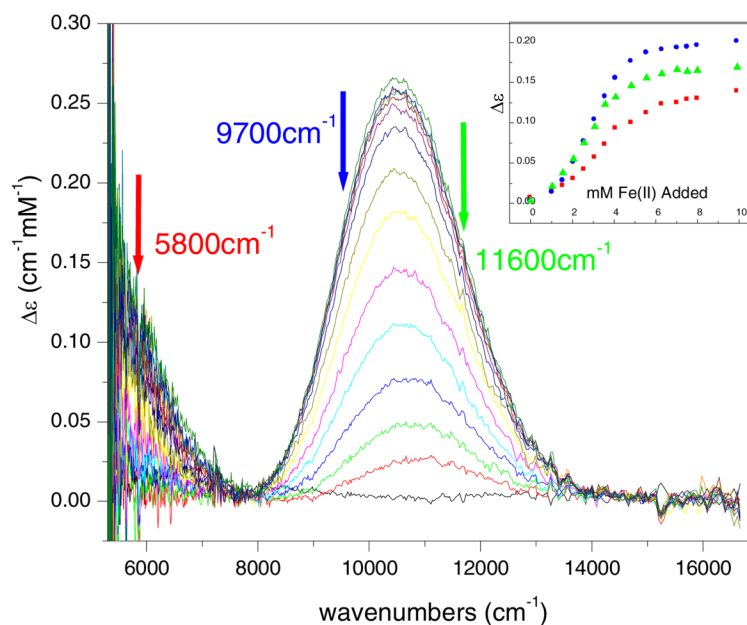
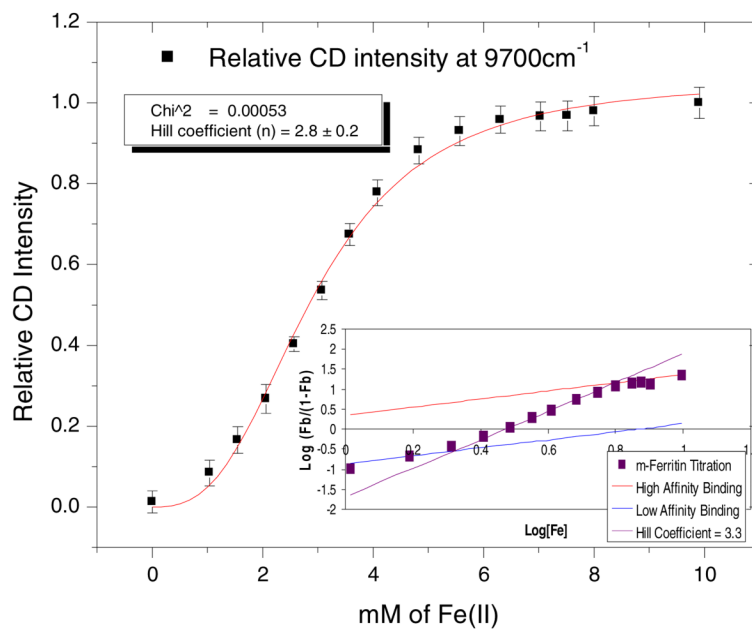


Figure 2.

CD spectra of M ferritin, recorded at 7°C, after the anaerobic addition of Fe(II). All features are saturated when 2 Fe(II) are added per ferroxidase site (spectrum in dark green) indicating both sites in the ferroxidase site should be occupied with Fe(II). Formation of the Fe(II) ferroxidase site in M ferritin is followed by CD data taken at 5800(red), 9700(blue), and 11 600 cm^{-1} (green). Positions are noted on the CD spectra and data are plotted in their respective colors in the inset. These energies were chosen to minimize overlap with the other transitions and obtain best signal to noise ratios, and are representative of each of the three transitions observed in CD.

**Figure 3.**

Each curve shown in the inset of Figure 2 was normalized and fit to $Y = [Fe]^n / (K^n + [Fe]^n)$ in Origin 6.0 using a non-linear Levenberg-Marquardt (LM) algorithm to minimize chi-squared. Fit to data at 9700 cm⁻¹ is shown; similar fits to the curve at 11600 and 5800 cm⁻¹ were obtained and are shown in Figure S2. Hill coefficients between 2.5 to 3.2 were obtained for all curves using this origin fitting method. A standard Log Hill plot for this data (inset) determines a Hill coefficient of 3.3, in close agreement with the previous fitting method. The Low affinity binding constant was determined to be $\sim 100 \text{ M}^{-1}$ and high affinity binding constant was $\sim 2.3 \times 10^3 \text{ M}^{-1}$.

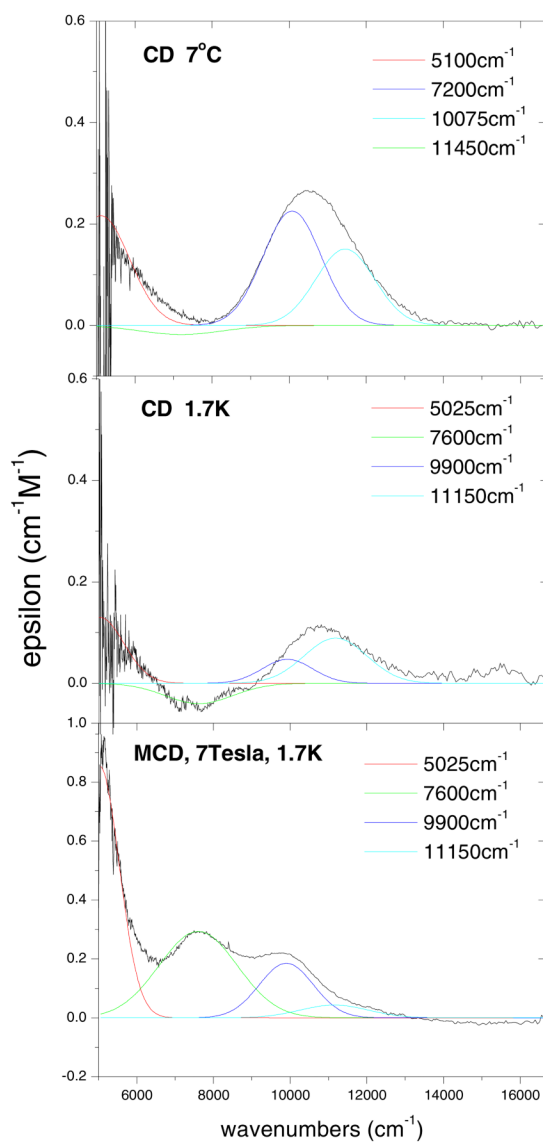
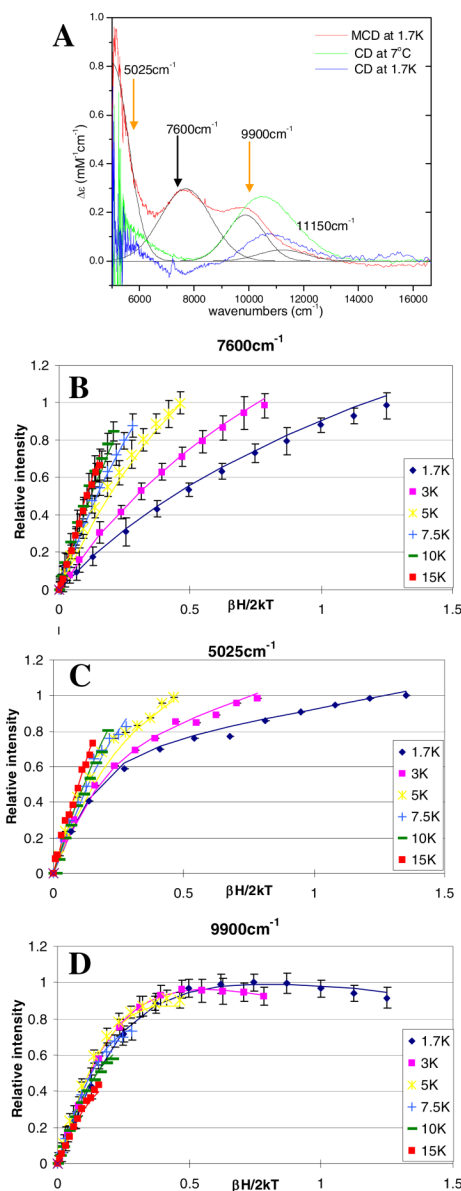
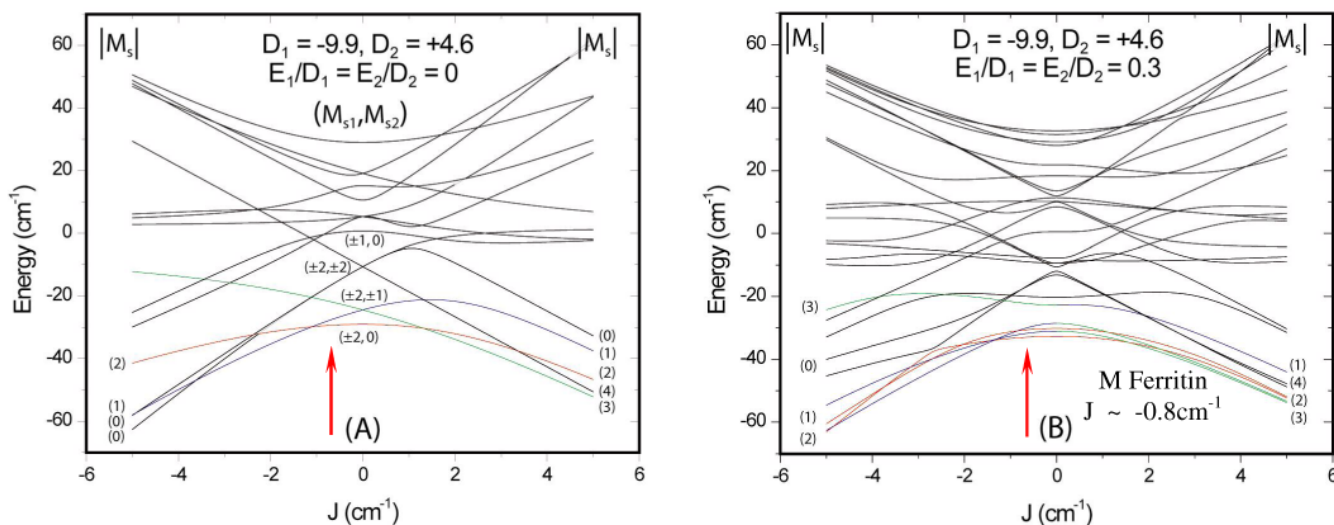


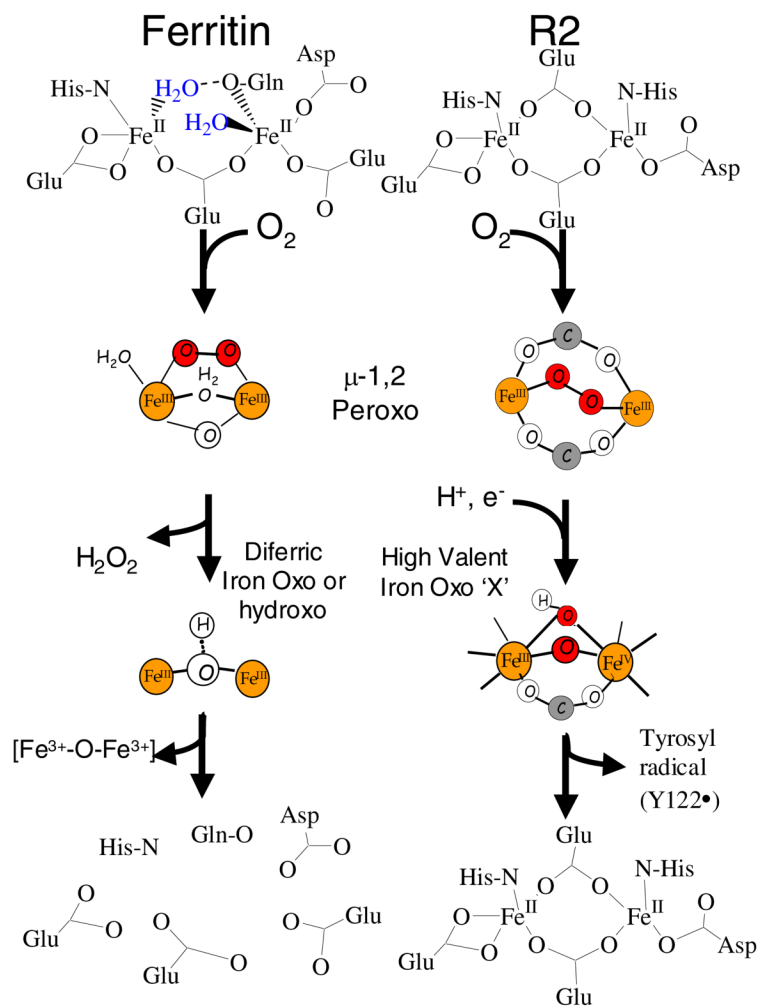
Figure 4. CD (7°C), Low Temp. CD (1.7K), and Low Temp. MCD (1.7K, 7Tesla) spectra of the Fe(II) Fe(II) active site in M ferritin. The experimental data (black) were simultaneously fit with individual Gaussian band shapes, shown in color.

**Figure 5.**

A: Overlay of CD (7°C) and Low Temp (1.7K) CD and MCD spectra. Gaussian Peak fit is shown in black. Peaks at 7600 and 11 150 cm^{-1} are assigned to Fe1 and peaks at 5025 and 9900 cm^{-1} are assigned to Fe2. Arrows indicate energies at which VTVH MCD data was taken. Intensity of the peak at 11 150 cm^{-1} is too small for acceptable VTVH data to be collected. Below this are Spin-Hamiltonian fits of this VTVH MCD data represented by solid line over WT-M ferritin data taken at (B) 7600 cm^{-1} (C) 5025 cm^{-1} and (D) 9900 cm^{-1} . Error bars for data at 5025 cm^{-1} have been omitted since they are too large for conclusive results, as this energy region is near the detection limit for this instrument; thus fits for this energy were only used to further support assignments. Fit parameters are summarized in Table 1 and 2.

**Figure 6.**

Correlation diagrams of the energy levels of the binuclear ferrous ground state with oppositely signed ZFS. The exchange coupling (J) is varied along the x-axis from -5 to $+5$ cm^{-1} . The pure ZFS limit is at $J = 0$ and is labeled with the M_{S_i} values for an uncoupled Fe(II). The right side indicates a ferromagnetic interaction ($J > 0$) between the Fe(II)'s and the left an anti-ferromagnetic interaction. Each side is labeled with the total $|M_S|$. The arrows indicate the J -value corresponding to the spin states determined for M ferritin. The spin Hamiltonian used for calculating the levels is given in eq 3, with (A) $D_1 = -9.9$ cm^{-1} , $D_2 = +4.6$ cm^{-1} , and $E_1 = E_2 = 0$ and (B) $D_1 = -9.9$ cm^{-1} , $D_2 = +4.6$ cm^{-1} , $E_1 = E_2 = 1/3|D|$. Relevant energy levels are colored according to the total $|M_S|$ (red = 2, blue = 1, and green = 3), or the dominant value in the case of the mixed sublevels in the rhombic system.

**Scheme 1.**

Left: proposed reaction pathway for M ferritin resulting in release of ferric-oxo mineral precursor from the active site, assuming equal rates of dioxygen binding and ET for all the types of diiron sites. The two bound waters may provide the protons necessary for formation of hydrogen peroxide. The water derived bridge present in the peroxo species may exist as a hydroxo or aquo bridge. Refs:13-17 **Right:** reaction pathway for R2 ribonucleotide reductase leading to a high valent intermediate and generation of a stable tyrosyl radical (Y122•). Refs: 4,8,11,24,58

Table 1

Summary of the ground and excited state parameters for Fe(II)Fe(II) substrate site in M ferritin as determined by fitting with the doublet model.

	M ferritin	
	G.S.	E.S.
g_{\parallel}	8	4
δ	4.3 ± 0.5	5.3 ± 0.5
Energy (cm^{-1})	0	3.4 ± 1

Table 2
Spin-Hamiltonian Parameters (from spin-projection model) for Fe(II)Fe(II) substrate site in M ferritin

	M ferritin		
MCD	9900 cm⁻¹	7600 cm⁻¹	5025 cm⁻¹
J (cm ⁻¹)	-0.9 ± .3	-0.8 ± .4	-0.8
D ₁ (cm ⁻¹)	-9.75 ± .5	+4.6 ± .5	-10
E ₁ /D ₁ (cm ⁻¹)	0.30	0.30	
D ₂ (cm ⁻¹)	+5 ± 2	-9 ± 2	5
%X	1	90	30
%Y	98	10	15
%Z	1	0	55

Table 3

Comparison of ground state and spectral parameters for the substrate ferroxidase site of M ferritin, and the cofactor sites in MmoH+MmoB bound complex, R2, and Δ^9 d+substrate complex

	m-Fr ^a	MMOH+MMOB ^b	R2 (<i>E. coli</i>) ^c	Δ^9 d+substrate ^d
g_{II} (ground)	8	16.2	8	~4
δ_I	4.3	.68	4.6	1.97
g_{II} (excited)	4	0	4	~8
E_{ESI} (cm ⁻¹)	~3.4	5	6	1.5
J (cm ⁻¹)	-0.8	+ 0.3 - 0.5	-0.44	-2.5
Fe1 : D1 (cm ⁻¹)	+ 5	-6	-10	-7
Coord.#/Transitions	5C: 7600, 11150	5C: 7590, 8650	5C: 9000	5C: 9650
Fe2: D2 (cm ⁻¹)	-10	-6	+5	+3
Coord.#/Transitions	5C : 5025, 9900	5C: 6170, 9840	4C: 7500, 5500	4C: 5000, 7900
λ_{max} (nm)	650	725	700	700
$\nu(O-O), \nu(Fe-O)_{sym}$	851, 485	--	870, 457	898, 442
$\Delta E_Q, \delta$	1.06, 0.62	1.51, 0.66	1.58, 0.63	1.9(1.06), 0.68(.64)

^athis work and refs 14,17

^brefs 2,10,26; MMOB perturbs the active site and increases the rate of O₂ reactivity by 1000 fold over MMOH alone

^crefs 3,4,8,24

^drefs 1,9,25; addition of substrate alters the 5C5C site to a 4C5C site and is required for efficient O₂ reactivity